processes

MDPI

Article

Quantitative Analysis of Heterogeneity Effects and Heat Transfer on Self-Diverting Acid Performance in Multi-Layered Carbonate Reservoirs

Jinwei Wu [1] and Fajian Nie [2,*]

[1] Oil Production Plant No. 1 of Sinopec North China Oil and Gas Branch, Xianyang 712000, China
[2] College of Petroleum Engineering, Yangtze University, Wuhan 430100, China
* Correspondence: cjdx0401@163.com

Abstract

The severe heterogeneity of carbonate reservoirs poses a significant challenge to matrix acidizing, making the achievement of uniform stimulation across multiple strata a persistent engineering difficulty. To address this, a numerical simulation program for self-diverting acid (SDVA) in multi-layered rocks was developed based on the two-scale continuum model and the open-source framework FMOT. This study primarily investigates the regulatory effects of heterogeneity intensity and initial temperature on uniform acidizing performance. The results indicate that, compared to conventional HCl, SDVA significantly enhances the uniform acidizing efficacy in low-permeability layers. Furthermore, SDVA induces a unique "competitive propagation" pattern among multi-layered rocks, which is fundamentally distinct from the fluid diversion behavior of HCl. As the formation heterogeneity intensity increases, the resulting wormhole morphology becomes increasingly complex, accompanied by more pronounced inter-layer flow competition. Moreover, unlike HCl, whose flow distribution pattern and wormhole morphology are insensitive to thermal changes, the acidizing performance of SDVA exhibits marked temperature dependence. At lower temperatures, the competitive propagation pattern diminishes significantly; however, as the temperature rises, the inter-layer fluid competition becomes progressively intensified, and this competitive state persists until the ultimate breakthrough of the rock matrix.

Keywords: fractured reservoirs; pre-flush stage; wormhole morphology; two-scale continuum model; embedded discrete fracture network model

Check for updates

Academic Editors: Daniel Asante Otchere and Bennet Nii Tackie-Otoo

Received: 12 May 2026
Revised: 12 June 2026
Accepted: 16 June 2026
Published: 29 June 2026

Copyright: © 2026 by the authors. Licensee MDPI, Basel, Switzerland. This article is an open access article distributed under the terms and conditions of the Creative Commons Attribution (CC BY) license.

1. Introduction

Carbonate reservoirs play an important role in the global energy supply. These reservoirs commonly contain natural fractures and marked heterogeneity. They are also susceptible to formation damage during drilling, completion, and production, which can reduce reservoir permeability. Matrix acidizing is widely used to stimulate carbonate reservoirs. In this process, injected acid reacts with and dissolves the rock matrix, forming conductive acid-etched wormholes [1–3].

Because wormhole morphology controls stimulation efficiency and conductivity enhancement, quantitative prediction of wormhole propagation remains an important research topic. In field applications, carbonate reservoirs often exhibit vertically layered structures with layer-to-layer variations in permeability and porosity. This interlayer heterogeneity can lead to uneven acid distribution. Conventional acid tends to preferentially enter

high-permeability layers, while low-permeability or damaged zones may receive insufficient acid. Temperature also affects acid-rock reaction kinetics and wormhole propagation. Self-diverting acid (SDVA) has therefore been proposed as a method for improving acid placement in heterogeneous reservoirs [4,5]. During acid spending, SDVA can increase in viscosity, modify subsequent flow paths, and promote diversion toward low-permeability zones [6,7]. Owing to its operational advantages and limited secondary formation damage, SDVA has been widely used in carbonate reservoir stimulation [8–12].

Extensive experimental studies have systematically revealed the key controlling factors of the acidizing process. Early core-flooding experiments defined five typical dissolution patterns (uniform dissolution, ramified wormholes, dominant wormholes, conical wormholes, and face dissolution) by varying injection rates and acid types. Subsequent research further confirmed that wormhole formation is primarily governed by acid-rock reaction kinetics [13], and particularly regarding heat transfer, temperature plays a decisive role in the acid-rock reaction rate [14]. Wang et al. [15] found that the optimal injection rate is massively influenced by temperature; Huang et al. [16] pointed out that elevated temperatures accelerate the acid-rock reaction and alter the dissolution patterns; and Sayed et al. [17,18] and Dong et al. [14,19] observed that under high-temperature conditions, increasing the injection rate tends to yield more complex and ramified wormhole morphologies. Additionally, the effect of temperature on the pore volume to breakthrough (PV_{BT}) exhibits complex nonlinear characteristics under different control mechanisms. Although these experiments have made significant progress in characterizing the heat transfer and mass transfer behaviors of simple heterogeneous cores [20,21], they struggle to fully capture the dynamic interlayer diversion of SDVA and the developmental process of wormhole branches when confronting the issue of uneven acid distribution caused by property variations in actual multi-layered systems.

Compared to the scale limitations and prohibitive costs of experiments, numerical simulation provides a more flexible and efficient approach for studying the acidizing process under complex reservoir conditions. Numerous simulations have demonstrated that variations in reservoir petrophysical properties critically impact dissolution patterns [22–24]. Panga et al. described the acidizing process at both the Darcy and pore scales. The Darcy scale was used to characterize macroscopic flow and reactive transport in porous media, whereas the pore scale was employed to capture the evolution of pore-scale microstructures induced by acid–rock reactions. Based on this multiscale description, they developed the Two-Scale Continuum (TSC) model [25]. Based on the TSC model, Yang et al. [26] found that stronger reservoir heterogeneity more readily generates narrow and densely branched wormholes, thereby altering the competitive growth dissolution mechanism. Regarding thermal effects, studies indicate that injecting cold acid at appropriate rates can enhance acidizing efficiency, and the optimal injection rate increases with rising temperatures [27–29]. Xue et al. [30] incorporated the impact of the molar heat of the acid–rock reaction, discovering that this exothermic reaction elevates the temperature at the wormhole tip by over 11 K, significantly altering the macroscopic dissolution morphology. Research by Wang et al. [31] and Samadi [32] further revealed the dissolution disparities of specific mineral components at different temperatures.

In summary, the classical TSC model of Panga et al. provides a rigorous framework for simulating wormhole propagation during carbonate matrix acidizing; however, it was mainly developed for single-core acidizing and does not explicitly resolve interlayer flow allocation in multi-layered carbonate reservoirs. Previous SDVA studies have improved the understanding of viscosity evolution, gelation behavior, and acid diversion capacity, but most of them focused on rheological tests, diversion mechanisms, or single-layer core behavior. As a result, the coupled relationship among SDVA gelation, wormhole

growth, gel-induced flow resistance, and interlayer flow redistribution has not been fully quantified. In addition, FMOT-based acidizing studies by Chang et al. advanced the numerical simulation of carbonate acidizing and wormhole development, whereas the combined effects of heterogeneity intensity and thermal conditions on uniform acidizing performance in multi-layered systems were not systematically evaluated. In contrast, the present study integrates the TSC acidizing framework with the FMOT implementation to establish an SDVA acidizing model for multi-layered carbonate reservoirs. This model explicitly couples temperature-dependent SDVA gelation, acid–rock reaction, wormhole propagation, gel-induced resistance evolution, and interlayer flow allocation, thereby providing a quantitative framework for evaluating self-diverting acid performance under the coupled effects of reservoir heterogeneity and heat transfer.

2. Mathematical Formulation

This section details a mathematical framework for simulating reactive transport and acid–rock reaction processes of HCl and SDVA in carbonate reservoirs, with particular emphasis on matrix acidizing mechanisms. This framework is divided into two parts: (1) the basic acid–rock reaction module, and (2) the SDVA gel zone module. Specifically, the first part incorporates a heat transfer model to describe the temperature changes in the solid matrix and fluid phase during acidizing.

(1) Basic acid–rock reaction module

The baseline acid–rock reactive transport module is formulated based on the Two-Scale Continuum (TSC) model. The model assumes single-phase, incompressible Darcy flow during acid injection. At the Darcy scale, the governing equations primarily comprise the following:

Pressure Equation: describes the macroscopic flow field for the acidizing system [5,25]:

$$-\nabla \cdot (\boldsymbol{K}\lambda \nabla P) = Q \tag{1}$$

where $\boldsymbol{K}$, λ, P, and Q are the permeability tensor, fluid mobility, pressure field, and source/sink term, respectively. Further, based on Darcy's law, the velocity of acid is [33]:

$$\boldsymbol{U} = -\boldsymbol{K}\lambda(\nabla P) \tag{2}$$

Here, λ is the single-phase mobility and is defined as $\lambda = 1/\mu_{\text{eff}}$, where μ_{eff} is the dynamically updated viscosity. For HCl, μ_{eff} remains equal to the acid viscosity. For SDVA, μ_{eff} is updated using the gel-zone viscosity model in Equation (11); therefore, viscosity evolution directly changes the pressure field and flow redistribution.

Heat transfer Equations: Capture the transient energy conservation for both the fluid and solid phases, accounting for convective heat transfer and the heat of the acid–rock reaction, the acid temperature equation is [33]:

$$\frac{\partial \phi \rho_l C_{p,l} T_l}{\partial t} + \nabla \cdot (\boldsymbol{U}_i \rho_l C_{p,l} T_l) = \nabla \cdot (\phi k_l \nabla T_l) + H_m a_v (T_r - T_l) \tag{3}$$

where ρ_l, $C_{p,l}$, and k_l denote the density, specific heat capacity, and thermal conductivity of the acid phase, respectively; T_l and T_r represent the macroscopic temperature fields of the liquid and rock; and H_m is the fluid–solid convective heat transfer coefficient. In this work, H_m is treated as a prescribed pore-scale heat-transfer coefficient with units of $\mathrm{W\,m^{-2}\,K^{-1}}$; the simulations use $H_m = 600\ \mathrm{W\,m^{-2}\,K^{-1}}$. The term $H_m a_v (T_r - T_l)$ therefore has units of $\mathrm{W\,m^{-3}}$, consistent with the volumetric energy balance. Viscous dissipation is neglected because the Darcy velocities considered in matrix acidizing are low and the heat

generated by viscous work is small compared with convective heat transfer and acid–rock reaction heat.

The rock temperature equation is [6,25]:

$$\frac{\partial(1-\phi)\rho_r C_{p,r} T_r}{\partial t} = \nabla \cdot ((1-\phi)k_r \nabla T_r) - H_m a_v (T_r - T_l) - \underbrace{\Delta H_r(T_r) a_v R(C_s)}_{\text{chemical reaction heat}} \quad (4)$$

where ϕ and a_v denote the macroscopic porosity and the specific interfacial area of the rock matrix, respectively. ρ_r, $C_{p,r}$, and k_r correspond to the density, specific heat capacity, and thermal conductivity of the solid rock matrix, respectively, while $\Delta H_r(T_r)$ and $R(C_s)$ define the temperature-dependent molar heat of the acid–rock reaction and the reaction consumption rate, respectively. The reaction heat is calculated as

$$\Delta H_r(T_r) = -13692 - 6.443 \times 10^{-3} T_r^2 + 16.075 T_r - \frac{17.406 \times 10^5}{T_r}, \quad (5)$$

where ΔH_r is in J mol^{-1} and T_r is in K. The product $\Delta H_r(T_r) a_v R(C_s)$ has units of W m^{-3}. The two temperature equations use a local thermal non-equilibrium description, in which the liquid and rock temperatures are solved separately and coupled through the interfacial heat-transfer term. Thus, thermal equilibrium between the pore fluid and the solid matrix is not imposed.

H^+ Transport Equation: Governs the convection, dispersion, and reactive consumption of the effective acid species (H^+) within the porous media:

$$\frac{\partial \phi C_f}{\partial t} + \nabla \cdot (\boldsymbol{U} C_f) = \nabla \cdot (\phi \boldsymbol{D}_e \cdot \nabla C_f) - R(C_s) a_v \quad (6)$$

where C_f and $\boldsymbol{D}_e$ represent its cup-mixing mass concentration and effective dispersion tensor, respectively.

Porosity Evolution Equation: Characterizes the dynamic growth of macroscopic porosity driven by mineral dissolution [25]:

$$\frac{\partial \phi}{\partial t} = \frac{R(C_s) a_v \alpha_c}{\rho_s} \quad (7)$$

where α_c is the dissolving power of the acid.

Concurrently, at the pore scale, the constitutive equations responsible for dynamically updating the transport and geometric properties include [25]:

$$\begin{aligned}
\frac{K_{new}}{K_{init}} &= \frac{\phi_{new}}{\phi_{init}} \left[\frac{\phi_{new}(1-\phi_{init})}{\phi_{init}(1-\phi_{new})} \right]^{2\beta} \\
\frac{r_{p,new}}{r_{p,init}} &= \sqrt{\frac{K_{new}\phi_{init}}{K_{init}\phi_{new}}} \\
\frac{a_{v,new}}{a_{v,init}} &= \frac{\phi_{new} r_{p,init}}{\phi_{init} r_{p,new}} \\
D_L^e &= \alpha_{os} D_m + \frac{2\lambda_L |\boldsymbol{U}| r_p}{\phi} \\
D_T^e &= \alpha_{os} D_m + \frac{2\lambda_T |\boldsymbol{U}| r_p}{\phi}
\end{aligned} \quad (8)$$

where $\boldsymbol{K}_{init}$ and ϕ_{init} denote the initial permeability and porosity fields, respectively, which remain strictly constant throughout the entire simulation. Furthermore, the effective dispersion tensor $\boldsymbol{D}_e$ is decomposed into longitudinal ($D_{e,L}$) and transverse components ($D_{e,T}$). $|\boldsymbol{U}|$ represents the velocity magnitude. α_{os}, λ_L, and λ_T are empirical constants

characterizing the pore structure. Further, similar to Panga's paper, $\alpha_{os} = 0.5$, $\lambda_L = 0.5$, and $\lambda_T = 0.1$ [25].

(2) SDVA gel zone module

The dissolution of carbonate rock by H^+ generates Ca^{2+} cations, which subsequently crosslink with the SDVA surfactant to form a high-viscosity gel zone. Accordingly, the governing equations for the gelation region include:

Ca^{2+} Transport Equation: Governs the convection, dispersion, and reactive generate of the effective acid species (Ca^{2+}) within the porous media [5]:

$$\frac{\partial \phi C_{Ca^{2+}}}{\partial t} + \nabla \cdot (\boldsymbol{U} C_{Ca^{2+}}) = \nabla \cdot (\phi \boldsymbol{D}_e \cdot \nabla C_{Ca^{2+}}) + 0.5 R(C_s) a_v \tag{9}$$

SDVA Transport Equation: Governs the convection and dispersion of the surfactants within the porous media [5]:

$$\frac{\partial \phi C_{\mathrm{SDVA}}}{\partial t} + \nabla \cdot (\boldsymbol{U} C_{\mathrm{SDVA}}) = \nabla \cdot (\phi \boldsymbol{D}_e \cdot \nabla C_{C_{\mathrm{SDVA}}}) \tag{10}$$

Dynamic Viscosity Equation for Gel Zone: Governs the viscosity changes in the gel region [5]:

$$\begin{aligned} \mu_{eff} = {} & \frac{\mu_0}{12}\left(9 + \frac{3}{n}\right)^n (150 K\phi)^{(1-n)/2} \\ & \times \left[\begin{array}{l} 1 + \frac{\mu_{\max}}{\mu_0} \exp\left(-0.5\left(\frac{C_{\mathrm{SDVA}} - C_{m,SDVA}}{W_1}\right)^2\right) \\ \times \exp\left(-\left(\frac{C_{Ca^{2+}} - C_{m,Ca^{2+}}}{W_2}\right)^2\right) \times \frac{(erf(bpH - c) + 1)}{W_3} \end{array} \right] \end{aligned} \tag{11}$$

where μ_0 and $\mu_{\max}$ denote the initial and maximum viscosities of the SDVA solution, with the latter set to 350 mPa·s (0.35 Pa·s). This viscosity relation is an empirical model adopted from previous SDVA rheology work rather than a newly developed constitutive law. The parameters $C_{m,Ca^{2+}}$ and $C_{m,\mathrm{SDVA}}$ represent the calcium and SDVA concentrations corresponding to peak viscosity, assigned values of 2.109 and 0.06, respectively. The parameters W_1 and W_2 control the concentration windows for SDVA and calcium, W_3 normalizes the pH-dependent term, and b and c control the slope and offset of the pH response. In this study, b, c, W_1, W_2, and W_3 are set to 1, 1, 0.0173, 1.1, and 2, respectively [4]. The pH used in Equation (11) is calculated from the hydrogen-ion concentration as

$$\mathrm{pH} = -\log_{10}(C_f) \tag{12}$$

3. Numerical Technique

In this section, the simulation strategy of the SDVA self-diverting acidizing in multi-layered carbonate reservoirs is introduced. The model in this paper is embedded in FMOT (https://github.com/FMOTs/FMOT_matlab, accessed on 2 October 2025), an open-source simulation framework developed by Chang [5,6,24].

4. Discrete Methods and Algebraic Equations

For the implicitly solved equations in both the fundamental acidizing and SDVA gel zone modules, the applied discretization schemes are as follows: backward Euler for the temporal term, first-order upwind for the convective term, and central difference for the Laplacian term. The resulting nonlinear systems are solved via the Newton–Raphson iterative method. The corresponding Jacobian matrices (**J**) and right-hand side residual vectors (**b**) are presented directly herein.

(1) Pressure Equation:

$$\begin{aligned} J_P &= A_{\mathrm{P}} + A_{\mathrm{N}} \\ A_{\mathrm{P}} &= \sum_{f\sim faces} \frac{\boldsymbol{K}_f}{\mu} \frac{|\boldsymbol{S}_f|}{|\boldsymbol{d}|} \\ A_{\mathrm{N}} &= -\sum_{f\sim faces} \frac{\boldsymbol{K}_f}{\mu} \frac{|\boldsymbol{S}_f|}{|\boldsymbol{d}|} \\ b_P &= 0 \end{aligned} \tag{13}$$

(2) Heat transfer Equations: The full coupled method is used to calculate the acid and rock temperature equations:

$$J_{T_{FC}} = \begin{bmatrix} J_{T_l} & J_{lr} \\ J_{rl} & J_{T_r} \end{bmatrix} \tag{14a}$$

$$\begin{aligned} J_{T_l} &= A_{\mathrm{P}} + A_{\mathrm{N}} + A^{\mathrm{up}} \\ A_{\mathrm{P}} &= V_{\mathrm{p}}\phi^t + \Delta t \sum_{f\sim faces} \phi_f^t k_l^t \frac{|\boldsymbol{S}_f|}{|\boldsymbol{d}|} + \Delta t V_{\mathrm{p}} H_m^t a_v^t \\ A_{\mathrm{N}} &= -\Delta t \sum_{f\sim faces} {\phi_f}^t k_l^t \frac{|\boldsymbol{S}_f|}{|\boldsymbol{d}|} \\ A^{\mathrm{up}} &= \Delta t \sum_{f\sim faces} \boldsymbol{F}_{l,f}^t \end{aligned} \tag{14b}$$

$$\begin{aligned} J_{T_r} &= A_{\mathrm{P}} + A_{\mathrm{N}} \\ A_{\mathrm{P}} &= V_{\mathrm{p}}(1-\phi)^t \rho_r^t C_{p,r}^t + \Delta t \sum_{f\sim faces} (1-\phi)_f^t k_{r,f}^t \frac{|\boldsymbol{S}_f|}{|\boldsymbol{d}|} + \Delta t V_{\mathrm{p}} H_m^t a_v^t \\ A_{\mathrm{N}} &= -\Delta t \sum_{f\sim faces} (1-\phi)_f^t k_{r,f}^t \frac{|\boldsymbol{S}_f|}{|\boldsymbol{d}|} \end{aligned} \tag{14c}$$

$$J_{lr} = J_{rl} = \Delta t V_{\mathrm{p}} H_m^t a_v^t \tag{14d}$$

$$b_{T_{FC}} = \begin{bmatrix} b_{T_l} \\ b_{T_r} \end{bmatrix} \tag{15a}$$

$$b_{T_l} = V_{\mathrm{p}}\phi^t T_{l,\mathrm{P}}^t + \Delta t V_{\mathrm{p}} H_m^t a_v^t T_{r,\mathrm{P}}^t \tag{15b}$$

$$\begin{aligned} b_{T_r} &= V_{\mathrm{p}}(1-\phi)^t \rho_r^t C_{p,r}^t T_{r,\mathrm{P}}^t + \Delta t V_{\mathrm{p}} H_m^t a_v^t T_l^t \\ &- V_{\mathrm{p}} \Delta H_r (T_{r,\mathrm{P}})^t a_v^t \frac{k_c^t k_s^t}{k_c^t + k_s^t} C_f^{t+\Delta t} \end{aligned} \tag{15c}$$

(3) H^+ Transport Equation:

$$\begin{aligned} J_{C_f} &= A_{\mathrm{P}} + A_{\mathrm{N}} + A^{\mathrm{up}} \\ A_{\mathrm{P}} &= V_{\mathrm{p}}\phi^t + \Delta t \sum_{f\sim faces} {\phi_f}^t \boldsymbol{D}_{e,f}^t \frac{|\boldsymbol{S}_f|}{|\boldsymbol{d}|} \\ A_{\mathrm{N}} &= -\Delta t \sum_{f\sim faces} {\phi_f}^t \boldsymbol{D}_{e,f}^t \frac{|\boldsymbol{S}_f|}{|\boldsymbol{d}|} \\ A^{up} &= \Delta t \sum_{f\sim faces} \boldsymbol{F}_f^t \\ b_{C_f} &= V_{\mathrm{p}}\phi^t C_{f,\mathrm{P}}^t - V_{\mathrm{p}} \Delta t a_v^t \frac{k_c^t k_s^t}{k_c^t + k_s^t} C_{f,\mathrm{P}}^t \end{aligned} \tag{16}$$

(4) Ca^{2+} Transport Equation:

$$\begin{aligned} J_{C_{Ca^{2+}}} &= A_P + A_N + A^{up} \\ A_P &= V_P \phi^t + \Delta t \sum_{f \sim faces} {\phi_f}^t \boldsymbol{D}_{e,f}^t \frac{|\boldsymbol{S}_f|}{|\boldsymbol{d}|} \\ A_N &= -\Delta t \sum_{f \sim faces} {\phi_f}^t \boldsymbol{D}_{e,f}^t \frac{|\boldsymbol{S}_f|}{|\boldsymbol{d}|} \\ A^{up} &= \Delta t \sum_{f \sim faces} \boldsymbol{F}_f^t \\ b_{C_{Ca^{2+}}} &= V_P \phi^t C_{Ca^{2+},P}^t + 0.5 V_P \Delta t a_v^t \frac{k_c^t k_s^t}{k_c^t + k_s^t} C_{f,P}^t \end{aligned} \tag{17}$$

(5) SDVA Transport Equation:

$$\begin{aligned} J_{C_{SDVA}} &= A_P + A_N + A^{up} \\ A_P &= V_P \phi^t + \Delta t \sum_{f \sim faces} {\phi_f}^t \boldsymbol{D}_{e,f}^t \frac{|\boldsymbol{S}_f|}{|\boldsymbol{d}|} \\ A_N &= -\Delta t \sum_{f \sim faces} {\phi_f}^t \boldsymbol{D}_{e,f}^t \frac{|\boldsymbol{S}_f|}{|\boldsymbol{d}|} \\ A^{up} &= \Delta t \sum_{f \sim faces} \boldsymbol{F}_f^t \\ b_{C_{SDVA}} &= 0 \end{aligned} \tag{18}$$

5. Solution Strategy

In this paper, the numerical simulation of uniform SDVA stimulation in multi-layered carbonate formations is achieved by adopting the Semi-Implicit Weak Coupling (SIWC) strategy proposed by Chang, coupled with a Proportional–Integral–Derivative (PID) controller for dynamic pressure regulation. The detailed computational workflow is illustrated in Figure 1, while the comprehensive mathematical derivations of the SIWC and PID algorithms can be found in Chang [6]; this section focuses solely on outlining the core calculation framework.

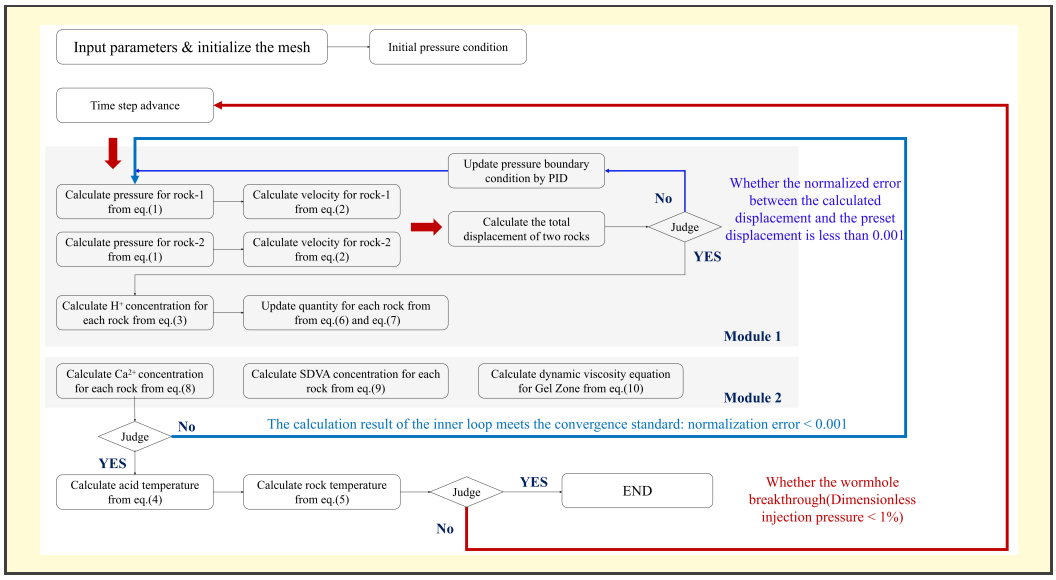

Figure 1. Solution Strategy Diagram.

6. Model Verification

To validate the accuracy of the developed simulator, our numerical results are compared against the benchmark case of the Two-Scale Continuum (TSC) model proposed by Panga et al. [25]. As shown in Figure 2, under the conditions of (a) Da $= 3 \times 10^4$, (b) Da $= 10^4$, (c) Da $= 500$, (d) Da $= 40$, and (e) Da $= 1$, the developed simulator successfully reproduces the five typical dissolution patterns, demonstrating excellent agreement with Panga's benchmark results. This consistency fully validates the accuracy and reliability of our numerical framework.

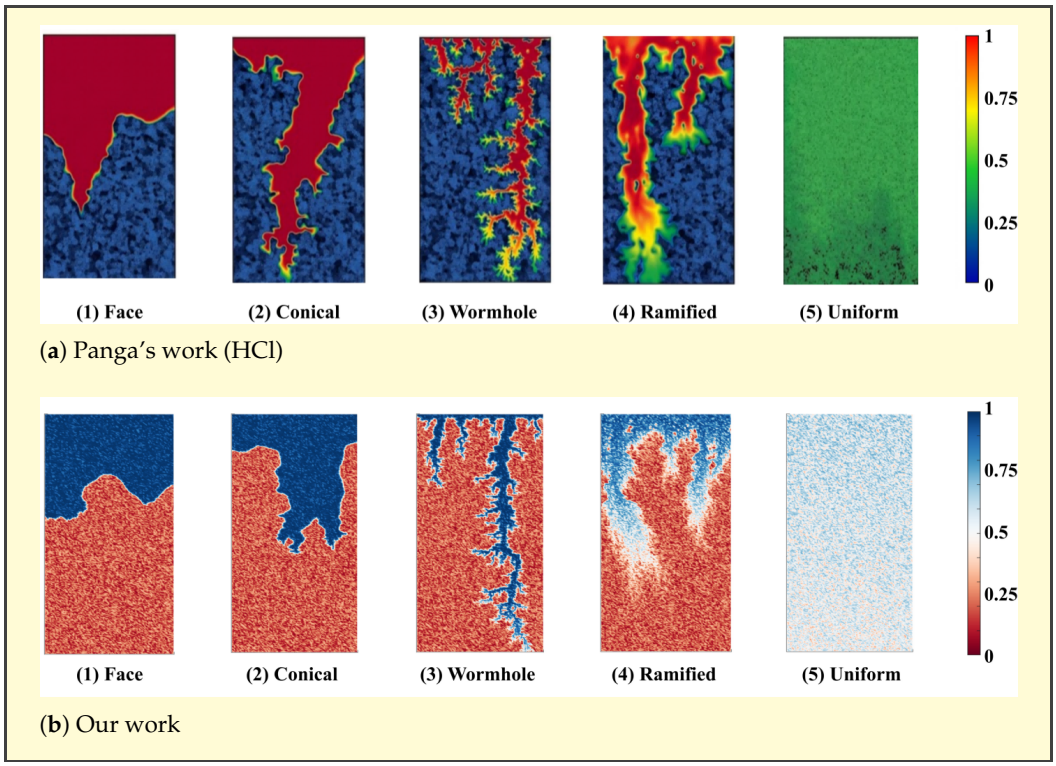

Figure 2. Model Validation Comparison between Benchmark Case of TSC and our simulator: (**a**) Panga's work and (**b**) Our work.

Figure 3 presents the PVBT values obtained by Panga for five dissolution patterns and compares them with the results of the current work. It can be seen that the present results are consistent with those of Panga in terms of both order of magnitude and overall trend. The minor discrepancies between the two sets of results mainly arise from the heterogeneous random distribution of porosity. Since Panga also adopted a random porosity field, differences between random realizations may inevitably lead to slight deviations in the calculated results.

Figure 4a presents the computational results reported by Liu. The pH value inside the wormhole is close to zero and gradually increases with distance from the wormhole. The distribution of Ca^{2+} exhibits an opposite trend to that of pH, indicating that the acid–rock reaction within the wormhole progressively propagates deeper into the core. The viscosity field shows a distribution pattern similar to that of Ca^{2+}. This is because fresh acid is continuously injected into the wormhole, while the spent acid is gradually displaced, forming a high-viscosity plugging zone around the wormhole. Figure 4b presents the computational results obtained using our simulator. Although the simulated wormhole morphology does not exactly reproduce Liu's result, the evolution trends of the physical fields are generally consistent.

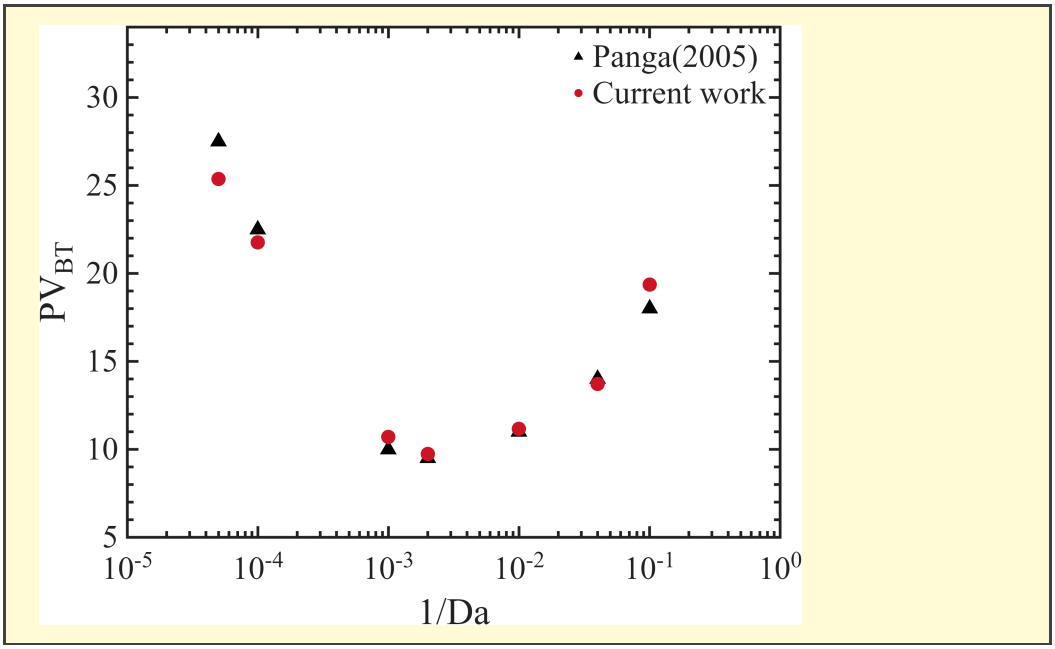

Figure 3. Comparison of pore volume of acid required to break through the core [25].

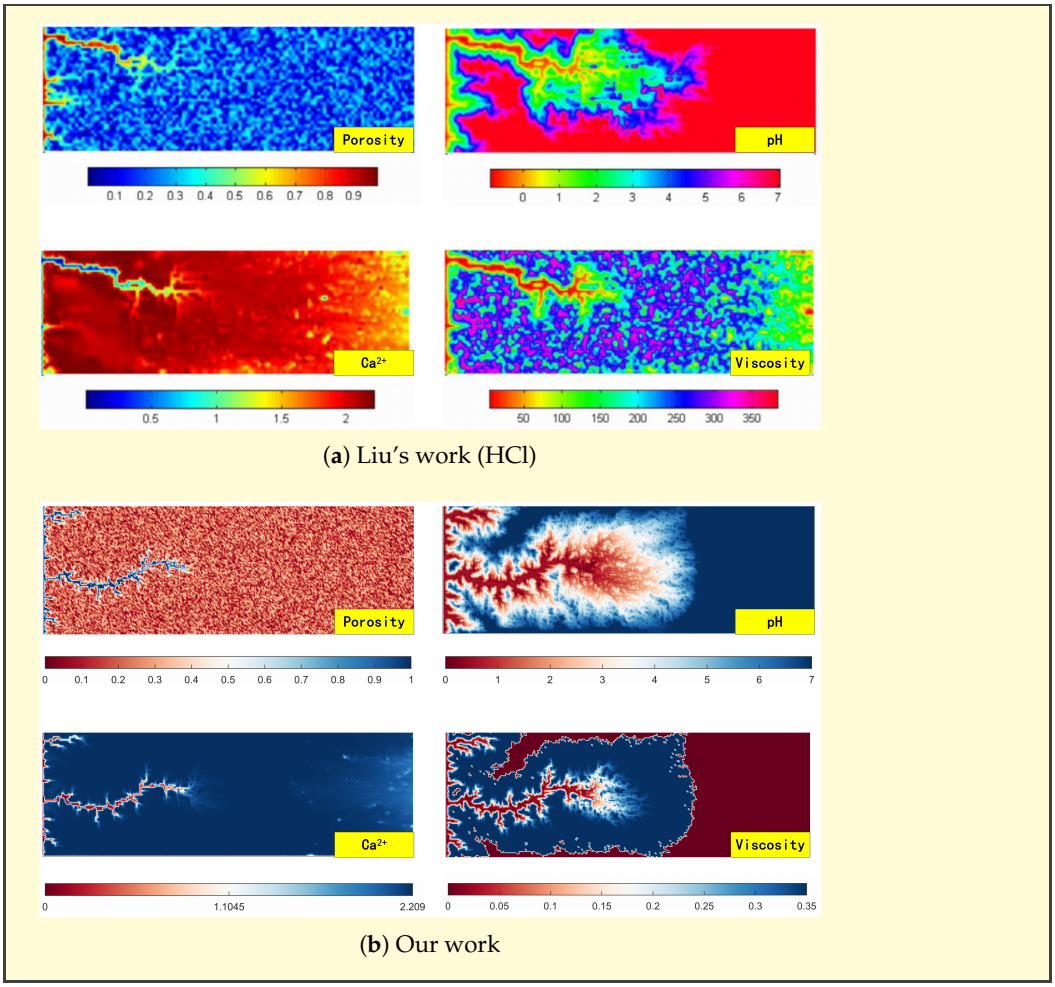

Figure 4. Verification results of SDVA: (**a**) Liu's work [34] and (**b**) Our work.

7. Results and Discussion

This section investigates the influence of heterogeneity intensity and thermal conditions on wormhole evolution during self-diverting acidizing in multi-layered rocks. Accordingly, the ensuing analysis is structured into two primary phases:

(1) Evaluating the morphological response to varying levels of heterogeneity, assuming a constant mean permeability and a static permeability contrast between adjacent layers.

(2) Analyzing how the initial acid temperature dictates treatment efficiency, evaluated strictly under the identical petrophysical constraints mentioned above.

Figure 5 displays the porosity field generated using normally distributed random numbers in this study. A uniform mean porosity and a consistent heterogeneity intensity are maintained across all rock layers. The heterogeneity is parameterized by the amplitude of porosity fluctuations and is stratified into three tiers: Low (L, [0.15, 0.25]), Medium (M, [0.10, 0.30]), and High (H, [0.05, 0.40]).

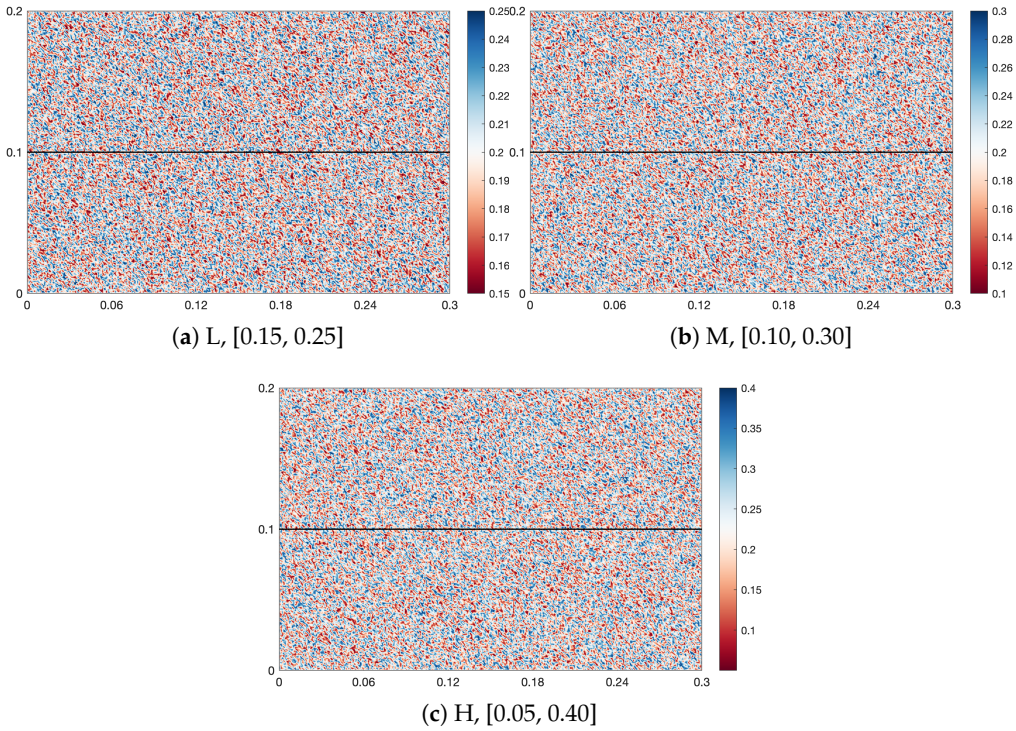

(**a**) L, [0.15, 0.25] (**b**) M, [0.10, 0.30]

(**c**) H, [0.05, 0.40]

Figure 5. Porosity distribution with three different heterogeneity intensities.

The Carman-Kozeny equation is used to calculate permeability through porosity [35]:

$$K = \frac{1}{72\chi} \frac{\phi^3 d_p^2}{(1-\phi)^2}, \tag{19}$$

where χ denotes an empirical Kozeny-type correction factor, and dp represents the pore diameter. In this paper, the χ is 0.81, and dp in high- and low-permeabilities is [1.85×10^{-5}, 1.62×10^{-5}, 1.07×10^{-5}] (mean permeability: 60 mD) and [2.14×10^{-5}, 1.88×10^{-5}, 1.23×10^{-5}] (mean permeability: 80 mD), respectively. The permeability distribution as shown in Figure 6.

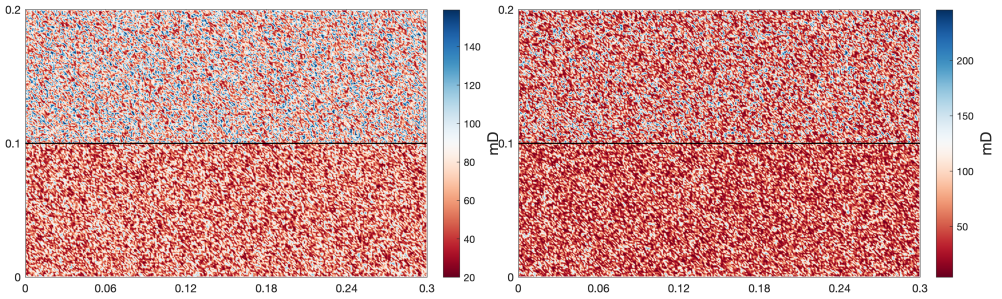

(**a**) L, [0.15, 0.25] (**b**) M, [0.10, 0.30]

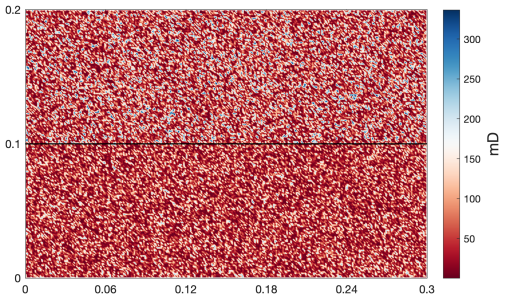

(**c**) H, [0.05, 0.40]

Figure 6. Permeability distribution with three different heterogeneity intensities.

7.1. Effect of Heterogeneity Intensity on Acidizing Performance

In this subsection, HCl is established as a control case to highlight the uniform acidizing performance of the self-diverting acid. The case parameter set in this section is shown in Table 1.

Table 1. Parameters of Case 1 to Case 6.

Parameters	**Case 1**	**Case 2**	**Case 3**	**Case 4**	**Case 5**	**Case 6**
Heterogeneity intensity	L	M	H	L	M	H
Acid type	HCl			SDVA		
Injection temperature [K]	333.15					
Displacement rate [m^3/s]	5×10^{-5}					

Figure 7 depicts the wormhole morphology resulting from each acid treatment under different heterogeneity conditions. The upper layer represents the high-permeability rock, whereas the lower layer represents the low-permeability rock. Both layers have the same dimensions of 0.3 × 0.1 m (L × H). At a low heterogeneity level (L), wormholes in both the upper and lower rock layers exhibit a classic "straight" morphology. Within the low-permeability layer, both HCl and SDVA generate two primary wormhole trunks. For HCl, these primary trunks produce minimal branching and exhibit negligible differences in propagation length. Conversely, SDVA develops distinct branches that propagate almost perpendicularly to the main trunk, with one primary trunk exhibiting highly dominant growth over the other. As the heterogeneity intensity increases to a moderate level (M), the wormholes in both layers maintain a generally "linear" propagation trajectory; however, they no longer manifest as simple straight channels but are instead accompanied by prominent branching. Two primary trunks continue to develop within the low-permeability rock, but the length discrepancy between the dual trunks for both HCl and SDVA is further minimized. Under high heterogeneity conditions (H), the wormhole morphology undergoes a fundamental transition from a "linear" to a "dendritic" pattern. This regime is characterized by significantly narrowed main trunks and the proliferation of abundant sec-

ondary branches. Furthermore, under such highly heterogeneous conditions, only a single, distinctly dominant wormhole trunk ultimately develops within the low-permeability layer.

Overall, the underlying mechanisms can be summarized as follows: At a Low (L) heterogeneity intensity, preferential flow paths within the rock matrix are not prominent; thus, HCl propagates in a straightforward manner. However, the gel zone formed near the propagating tips of SDVA forces the acid to divert locally, stimulating the development of elongated branches. As heterogeneity increases (at M and H levels), preferential flow paths become increasingly pronounced, and the discrepancy in flow resistance among pores enlarges significantly. This induces continuous divergence and splitting of the acidic fluid. The gelation effect of SDVA further amplifies this flow-resistance discrepancy, ultimately driving the evolution of highly complex wormhole configurations.

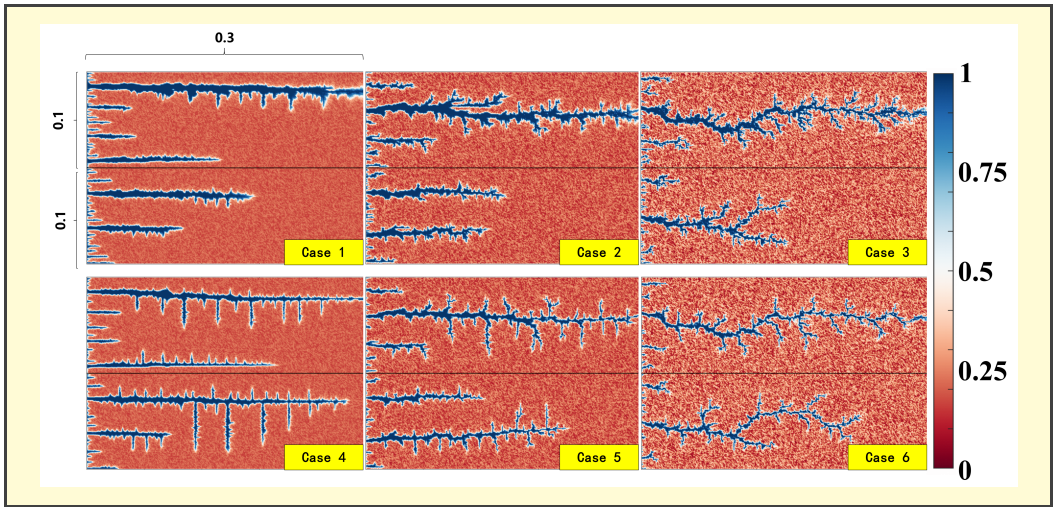

Figure 7. Wormhole morphology of Case 1 to Case 6.

Figure 8 presents a comparison of the fluid diversion profiles for the two acid systems across rock layers with differing permeabilities, revealing significant discrepancies in flow distribution. The vertical axis represents the fraction of the total injected flow allocated to the upper and lower layers under constant-rate injection, with the two fractions summing to unity. The horizontal axis denotes the cumulative volume of injected acid. For conventional HCl, the fractional flow allocated to the high-permeability layer remains substantially higher than that to the low-permeability layer throughout the entire acidizing process. As dissolution progresses, the preferential propagation of dominant wormholes in the high-permeability layer continuously suppresses fluid entry into the low-permeability rock, causing its fractional flow to decay steadily toward zero. Although intra-layer heterogeneity does not alter this fundamental diversion regime, it effectively retards the decay rate of the low-permeability layer's fractional flow.

During HCl matrix acidizing, the flow fraction allocated to the high-permeability layer remains consistently higher than that allocated to the low-permeability layer. Compared with HCl, SDVA exhibits a more complex diversion behavior, characterized by pronounced variations in the flow fractions of the two layers. At certain stages, the flow fraction allocated to the low-permeability layer exceeds that allocated to the high-permeability layer. This alternating change in the dominant flow allocation between layers is defined as the alternating competitive propagation pattern. The accelerated acid–rock reaction in the high-permeability layer promotes the rapid formation of a high-viscosity gel zone near the propagating wormhole tips, leading to a substantial increase in local flow resistance. This gel-induced supplementary resistance effectively bridges the initial permeability contrast between the layers. Consequently, at certain stages, the overall flow resistance

in the low-permeability layer drops below that of the high-permeability layer, allowing it to temporarily capture a dominant fraction of the injected flow. The stronger the initial heterogeneity, the more pronounced this alternating fluid diversion phenomenon becomes, as shown in Figure 8f.

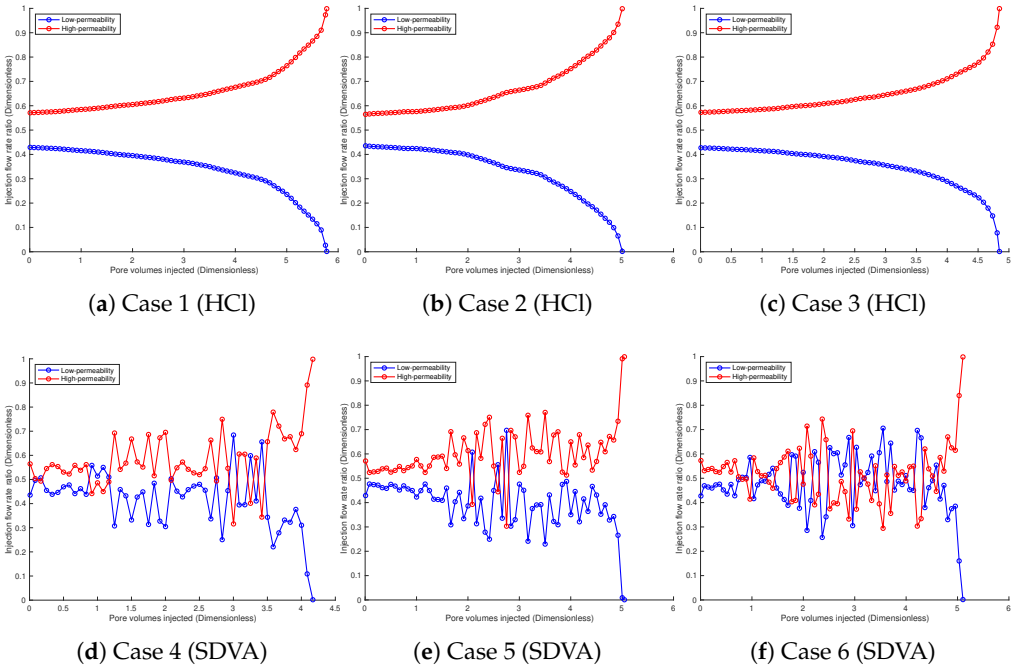

(**a**) Case 1 (HCl) (**b**) Case 2 (HCl) (**c**) Case 3 (HCl)

(**d**) Case 4 (SDVA) (**e**) Case 5 (SDVA) (**f**) Case 6 (SDVA)

Figure 8. Effect of different heterogeneity intensities on flow diversion: high-permeability core (upper layer) and low-permeability core (lower layer).

To more clearly compare the morphological complexity of wormholes formed under different heterogeneity conditions and acid systems, a dimensionless index is defined as

$$I_b = \frac{V_{\text{branch}}}{V_{\text{main}} + V_{\text{branch}}} \tag{20}$$

where V_{main} and V_{branch} represent the volumes of the main wormhole trunk and secondary branches, respectively. A larger I_b indicates a higher proportion of wormhole branches and therefore a more complex wormhole morphology. Figure 9 compares the wormhole complexity of HCl and SDVA under different reservoir heterogeneity conditions. The results show that the wormhole complexity generated by both acid systems increases as reservoir heterogeneity becomes stronger. Under low heterogeneity (L), the complexity index of SDVA is 0.40, higher than that of HCl at 0.31. As heterogeneity further increases, the wormhole complexity of SDVA remains higher than that of HCl. Under high heterogeneity (H), the complexity index of SDVA reaches 0.63, slightly higher than that of HCl at 0.61. This indicates that SDVA is more favorable for promoting branch development, thereby forming a more complex acid-etched channel structure.

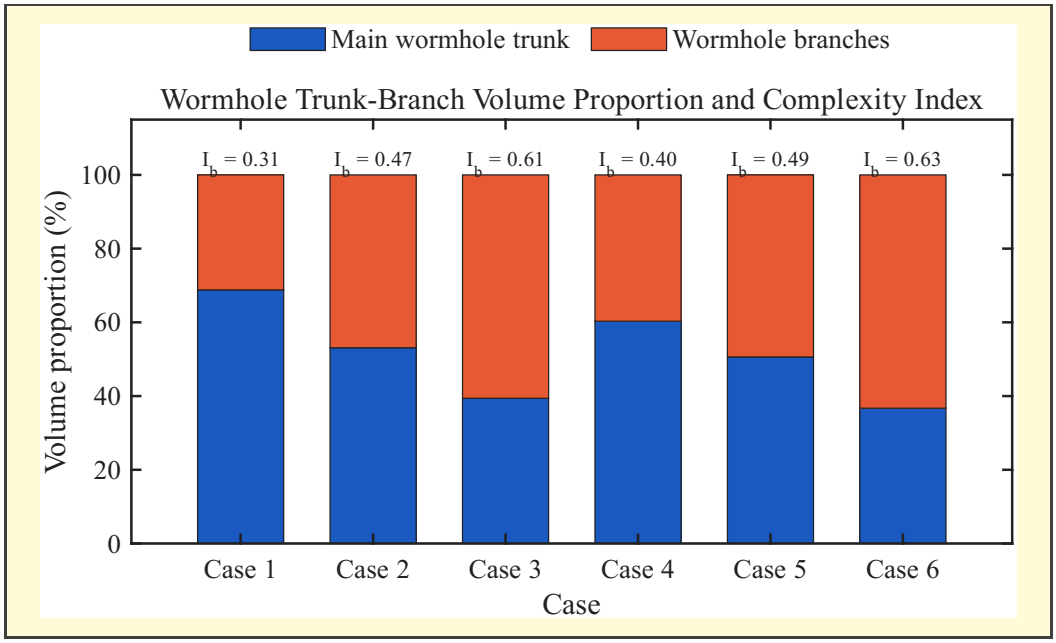

Figure 9. The impact of heterogeneity on the complexity of wormholes.

7.2. Effect of Acid Temperature on Acidizing Performance

This subsection further investigates the effect of acid temperature on acidizing performance. Similar to Section 7.1, HCl is established as the control group. The case parameter set in this section is shown in Table 2.

Table 2. Parameters of Case 7 to Case 12.

Parameters	Case 7	Case 8	Case 9	Case 10	Case 11	Case 12
Injection temperature [K]	293.15	313.15	353.15	293.15	313.15	353.15
Heterogeneity intensity	H					
Acid type	HCl			SDVA		
Displacement rate [m^3/s]	5×10^{-5}					

Figure 10 illustrates the temperature sensitivity of the wormholes generated by the two acid systems in multi-layered rocks. For HCl, temperature sensitivity is primarily reflected in the wormhole width: higher temperatures yield wider main trunks (e.g., the width at 353.15 K is significantly greater than at 293.15 K). Concurrently, the length of the main trunk in the lower layer progressively decreases as the temperature rises. This occurs because elevated temperatures accelerate the acid–rock reaction rate, thereby further amplifying the fluid-channeling advantage within the high-permeability rock.

In contrast, the main trunk width of SDVA wormholes lacks significant temperature sensitivity; the widths remain virtually identical across both high- and low-permeability layers under all three thermal conditions. However, the wormhole morphology within the low-permeability layer demonstrates pronounced temperature-dependent behavior. At 293.15 K, the relatively slow acid–rock reaction retards the development of the high-viscosity gel zone in the high-permeability layer. Consequently, the additional resistance induced by this gel is insufficient to substantially mitigate the flow resistance disparity between the two layers, resulting in a significantly shorter wormhole in the low-permeability layer compared to those at 313.15 K and 353.15 K. As the temperature increases, the accelerated gelation process effectively diverts the acid, allowing the wormhole length in the low-permeability layer to closely approach that in the high-permeability layer.

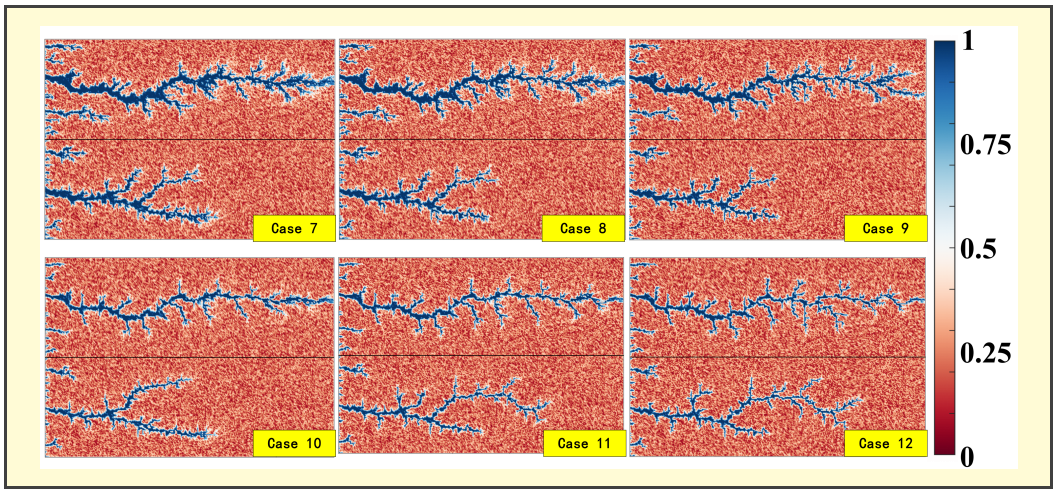

Figure 10. Wormhole morphology of Case 7 to Case 12.

Figure 11 illustrates the temperature sensitivity of the flow distribution curves for the two acid systems. The flow distribution pattern of HCl is not fundamentally altered by temperature variations; however, higher temperatures accelerate the breakthrough in the high-permeability rock, which consequently causes a more rapid decline in the fractional flow diverted to the low-permeability layer.

In contrast, the flow distribution evolution of SDVA shows marked sensitivity to temperature. At 293.15 K, although the flow allocation between the two layers exhibits marked fluctuations, the flow fraction assigned to the low-permeability rock remains predominantly lower than that of the high-permeability rock, indicating the absence of obvious competitive propagation. As the temperature rises, the flow competition between the upper and lower layers becomes more pronounced. For instance, at 353.15 K, this sustained fluid competition persists until the ultimate breakthrough of the rock matrix.

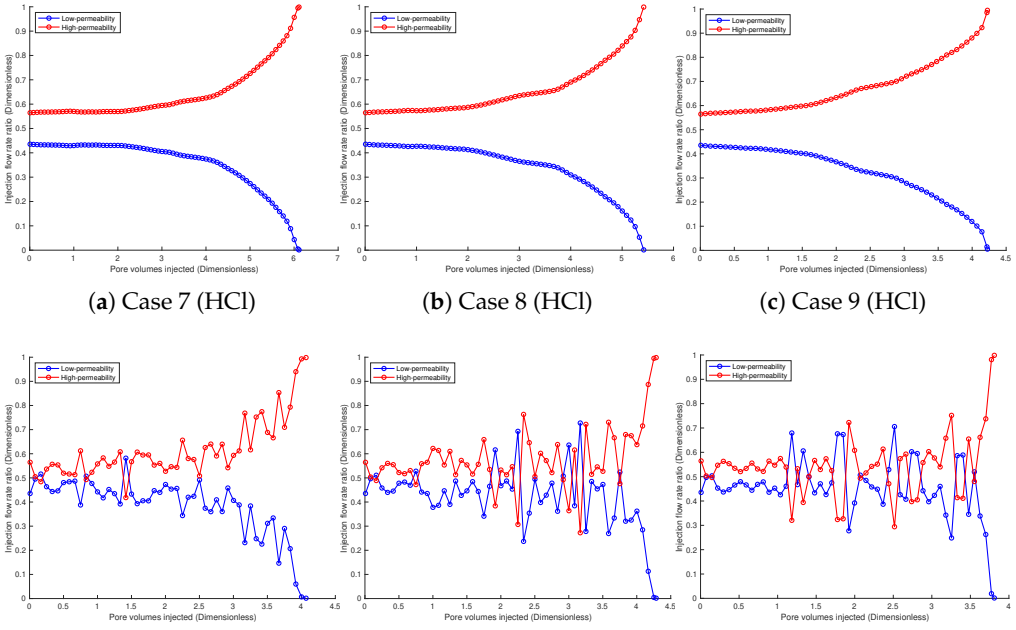

(**a**) Case 7 (HCl) (**b**) Case 8 (HCl) (**c**) Case 9 (HCl)

(**d**) Case 10 (SDVA) (**e**) Case 11 (SDVA) (**f**) Case 12 (SDVA)

Figure 11. Effect of different inject temperature on the flow diversion: high-permeability core (upper layer) and low-permeability core (lower layer).

Figure 12 illustrates the effect of acid injection temperature on wormhole complexity. Under the three tested temperatures, the wormhole complexity of HCl is 0.60, 0.61,

and 0.61, respectively, whereas that of SDVA increases from 0.62 to 0.63 and 0.65. This indicates that increasing temperature has only a limited influence on the complexity of HCl-induced wormholes, but it significantly enhances the complexity of SDVA-induced wormholes. The higher acid–rock reaction rate at elevated temperatures promotes the faster development of the dynamic gel zone, thereby strengthening the temporary plugging and diversion capability.

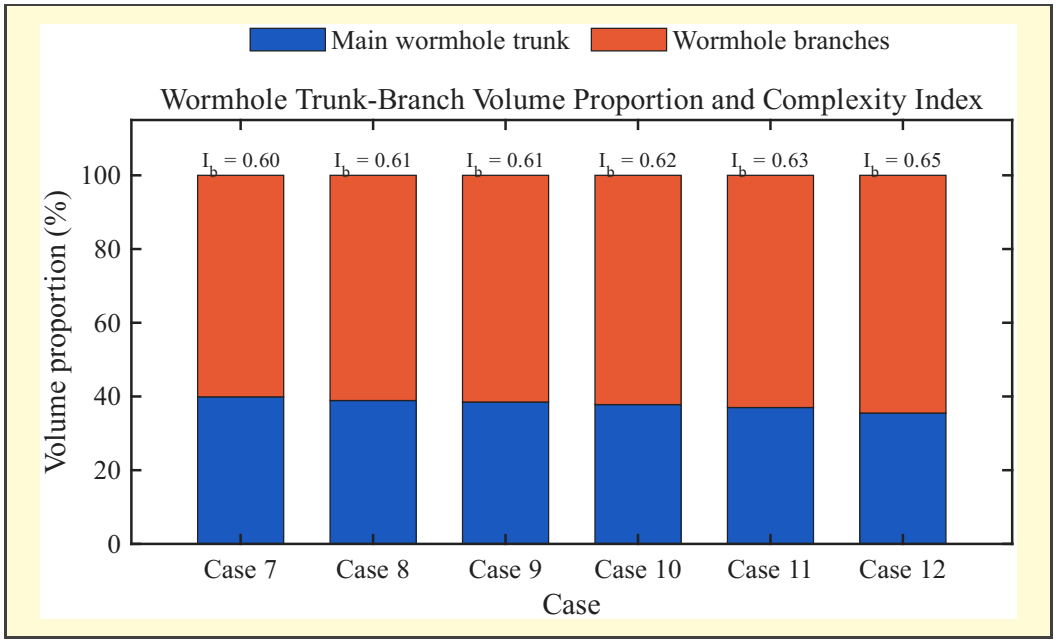

Figure 12. The impact of temperature on the complexity of wormholes.

8. Conclusions

In this study, the SIWC-SDVA-PID numerical simulation framework was employed to investigate the uniform acidizing capabilities of self-diverting acid (SDVA) in multi-layered rocks. Using straight HCl as a baseline for comparison, we systematically evaluated the comprehensive effects of heterogeneity intensity and acid temperature on the overall stimulation performance. By analyzing both the wormhole propagation morphologies and the dynamic flow distribution patterns, this work specifically elucidates the efficacy and mechanisms of SDVA in achieving uniform acidizing across highly heterogeneous strata. The primary conclusions are drawn as follows:

(1) Compared with conventional HCl, SDVA improves uniform acidizing in multi-layered rocks. SDVA promotes the formation of a high-viscosity gel zone near the propagating wormhole tips, which increases local flow resistance. This mechanism leads to an alternating competition pattern in the flow distribution between layers. As the heterogeneity intensity increases, the fluctuations in flow allocation between the high- and low-permeability rocks become more evident.

(2) The two acid systems show different sensitivities to initial temperature. For conventional HCl, elevated temperature mainly increases the main wormhole width. The accelerated acid–rock reaction also enhances preferential flow in the high-permeability layer, causing the wormhole penetration length in the low-permeability layer to decrease as temperature rises. For SDVA, the main trunk width shows limited sensitivity to temperature, whereas propagation length and branch development within the low-permeability layer show a clear temperature dependence.

(3) Temperature directly dictates the fluid competition and diversion efficiency of SDVA in multi-layered rocks by altering the gelation kinetics. At lower temperatures (e.g.,

293.15 K), the sluggish acid–rock reaction delays the development of the high-viscosity gel zone in the high-permeability layer. Consequently, it fails to effectively mitigate the inter-layer flow resistance disparity, resulting in a lack of prominent competitive propagation. As the temperature increases, the accelerated gelation process provides robust local plugging and diversion capabilities. This intensifies the fluid competition between the upper and lower layers, sustaining it until the ultimate breakthrough of the formation, and ultimately enabling the wormhole length in the low-permeability layer to closely approach that of the high-permeability layer.

From an engineering perspective, the results suggest that SDVA treatment design in multi-layered carbonate reservoirs should account for both permeability contrast and formation temperature. Higher temperatures may improve SDVA diversion by accelerating gel-zone development, whereas low-temperature treatments may require adjustment of acid concentration, injection rate, or SDVA formulation to achieve comparable diversion. For practical field application, the simulated inter-layer flow competition and wormhole propagation trends can provide guidance for identifying zones that are likely to be under-stimulated and for optimizing acid placement strategies before treatment. When extending the present core-scale model to field-scale acidizing design, scale-up effects should be considered carefully, including reservoir-thickness variation, wellbore injection distribution, radial flow geometry, larger-scale permeability architecture, operational limits on pumping rate and pressure, and uncertainty in in situ temperature and fluid properties. Therefore, model parameters should be calibrated using laboratory core-flooding results and, where available, field treatment data such as pressure response, production response, and post-treatment evaluation. The present model also has several limitations. It assumes single-mineral carbonate dissolution, neglects precipitation and pore collapse, and represents SDVA rheology using an empirical viscosity model. In addition, the validation focuses mainly on benchmark wormhole morphology; further quantitative validation against experimental measurements of breakthrough pore volume, pressure drop, and SDVA viscosity evolution is required in future work.

Author Contributions: Conceptualization, J.W. and F.N.; methodology, J.W. and F.N.; software, J.W. and F.N.; validation, J.W. and F.N., J.W. and F.N.; formal analysis, J.W. and F.N.; investigation, J.W. and F.N.; resources, J.W. and F.N.; data curation, J.W. and F.N.; writing—original draft preparation, J.W. and F.N.; writing—review and editing, J.W. and F.N.; visualization, J.W. and F.N.; supervision, J.W. and F.N.; project administration, J.W. and F.N.; funding acquisition, J.W. and F.N. All authors have read and agreed to the published version of the manuscript.

Funding: This research received no external funding.

Data Availability Statement: The original contributions presented in this study are included in the article. Further inquiries can be directed to the corresponding author.

Conflicts of Interest: Author Jinwei Wu was employed by the Oil Production Plant No. 1 of Sinopec North China Oil and Gas Branch. The remaining author declares that the research was conducted in the absence of any commercial or financial relationships that could be construed as a potential conflict of interest.

Nomenclature

Symbol	Description	Unit
Nomenclature of core flow variables		
$\boldsymbol{K}$	Permeability tensor of porous rock	m^2
K	Scalar permeability	m^2
$\boldsymbol{K}_f$	Permeability evaluated on grid face f	m^2
K_{init}	Initial permeability	m^2

K_{new}	Updated permeability after dissolution	m^2
λ	Fluid mobility; for single-phase flow, commonly $1/\mu$	$\text{Pa}^{-1}\ \text{s}^{-1}$
μ	Dynamic viscosity of the acid solution	Pa s
P	Pressure field	Pa
Q	Source or sink term in the pressure equation	s^{-1}
$\boldsymbol{u}$	Darcy velocity of the acid phase	m s^{-1}
$\boldsymbol{u}_i$	Darcy velocity used in the liquid-phase energy equation	m s^{-1}
Nomenclature of porosity, geometry, and pore-structure variables		
ϕ	Macroscopic porosity	dimensionless
ϕ_{init}	Initial porosity	dimensionless
ϕ_{new}	Updated porosity after dissolution	dimensionless
ϕ_f	Porosity evaluated on grid face f	dimensionless
a_v	Specific interfacial area of the rock matrix	m^{-1}
$a_{v,\text{init}}$	Initial specific interfacial area	m^{-1}
$a_{v,\text{new}}$	Updated specific interfacial area after dissolution	m^{-1}
r_p	Pore radius	m
$r_{p,\text{init}}$	Initial pore radius	m
$r_{p,\text{new}}$	Updated pore radius after dissolution	m
β	Empirical exponent in the permeability-porosity relationship	dimensionless
χ	Empirical Kozeny-type correction factor	dimensionless
d_p	Characteristic pore or particle diameter used in the Carman-Kozeny equation	m
α_{os}	Empirical pore-structure coefficient for molecular diffusion	dimensionless
λ_L	Empirical longitudinal dispersivity coefficient	dimensionless
λ_T	Empirical transverse dispersivity coefficient	dimensionless
Nomenclature of thermal, transport, and reaction variables		
T_l	Macroscopic temperature field of the liquid acid phase	K
T_r	Macroscopic temperature field of the rock phase	K
ρ_l	Density of the liquid acid phase	kg m^{-3}
ρ_r	Density of the rock matrix	kg m^{-3}
$C_{p,l}$	Specific heat capacity of the liquid acid phase	$\text{J kg}^{-1}\ \text{K}^{-1}$
$C_{p,r}$	Specific heat capacity of the rock matrix	$\text{J kg}^{-1}\ \text{K}^{-1}$
k_l	Thermal conductivity of the liquid acid phase	$\text{W m}^{-1}\ \text{K}^{-1}$
k_r	Thermal conductivity of the rock matrix	$\text{W m}^{-1}\ \text{K}^{-1}$
H_m	Fluid–solid convective heat-transfer coefficient	$\text{W m}^{-2}\ \text{K}^{-1}$
$\Delta H_r(T_r)$	Temperature-dependent molar heat of the acid–rock reaction	J mol^{-1}
C_f	Cup-mixing concentration of the reactive acid species H^+	mol m^{-3}
C_s	Surface concentration of the reactive acid species at the rock-fluid interface	mol m^{-3}
$R(C_s)$	Acid–rock reaction consumption rate as a function of C_s	$\text{mol m}^{-2}\ \text{s}^{-1}$
$\boldsymbol{D}_e$	Effective dispersion tensor	$\text{m}^2\ \text{s}^{-1}$
D_L^e	Longitudinal component of the effective dispersion tensor	$\text{m}^2\ \text{s}^{-1}$
D_T^e	Transverse component of the effective dispersion tensor	$\text{m}^2\ \text{s}^{-1}$
D_m	Molecular diffusion coefficient	$\text{m}^2\ \text{s}^{-1}$
α_c	Dissolving power of the acid	kg mol^{-1}
k_c	Acid–rock surface reaction-rate coefficient	m s^{-1}
k_s	Mass-transfer coefficient between bulk fluid and the rock-fluid interface	m s^{-1}
Nomenclature of SDVA gel-zone variables		
$C_{Ca^{2+}}$	Concentration of calcium ions generated by carbonate dissolution	mol m^{-3}
C_{SDVA}	Concentration or mass fraction of self-diverting acid surfactant	model-dependent
μ_{eff}	Effective dynamic viscosity in the SDVA gel zone	Pa s
μ_0	Initial viscosity of the SDVA solution	Pa s
$\mu_{\max}$	Maximum viscosity of the SDVA solution	Pa s
n	Power-law flow behavior index in the gel-zone viscosity model	dimensionless
$C_{m,Ca^{2+}}$	Calcium concentration corresponding to peak gel viscosity	mol m^{-3}
$C_{m,\text{SDVA}}$	SDVA concentration corresponding to peak gel viscosity	same as C_{SDVA}

W_1	Empirical width parameter for the SDVA concentration dependence of viscosity	same as C_{SDVA}
W_2	Empirical width parameter for the calcium concentration dependence of viscosity	mol m^{-3}
W_3	Empirical normalization parameter for the pH-dependent viscosity term	dimensionless
b	Empirical coefficient in the pH-dependent viscosity term	dimensionless
c	Empirical offset in the pH-dependent viscosity term	dimensionless
pH	Acidity of the reacting acid solution	dimensionless
$\mathrm{erf}(\cdot)$	Gaussian error function used in the pH-dependent viscosity term	dimensionless
Nomenclature of Jacobian and residual variables		
$\mathbf{J}$	Jacobian matrix of the nonlinear algebraic system	equation-dependent
J_P	Jacobian block for the pressure equation	equation-dependent
$J_{T_{FC}}$	Fully coupled Jacobian block for liquid and rock temperature equations	equation-dependent
J_{T_l}	Jacobian block for the liquid temperature equation	equation-dependent
J_{T_r}	Jacobian block for the rock temperature equation	equation-dependent
J_{lr}	Coupling Jacobian block from rock temperature to liquid temperature	equation-dependent
J_{rl}	Coupling Jacobian block from liquid temperature to rock temperature	equation-dependent
J_{C_f}	Jacobian block for H^+ transport	equation-dependent
$J_{C_{Ca^{2+}}}$	Jacobian block for calcium-ion transport	equation-dependent
$J_{C_{SDVA}}$	Jacobian block for SDVA transport	equation-dependent
$\mathbf{b}$	Right-hand-side residual vector of the nonlinear algebraic system	equation-dependent
b_P	Residual vector for the pressure equation	equation-dependent
b_{T_l}	Residual vector for the liquid temperature equation	equation-dependent
b_{T_r}	Residual vector for the rock temperature equation	equation-dependent
b_{C_f}	Residual vector for H^+ transport	equation-dependent
$b_{C_{Ca^{2+}}}$	Residual vector for calcium-ion transport	equation-dependent
$b_{C_{SDVA}}$	Residual vector for SDVA transport	equation-dependent
Nomenclature of discretization and performance variables		
A_P	Diagonal accumulation and diffusion coefficient associated with the primary cell	equation-dependent
A_N	Off-diagonal coefficient associated with neighboring cells	equation-dependent
A^{up}	Upwind convective contribution	equation-dependent
V_p	Volume of the primary control volume or grid cell in the discrete equations	m^3
Δt	Time-step size	s
$\boldsymbol{S}_f$	Area vector of grid face f	m^2
$\boldsymbol{d}$	Distance vector between neighboring cell centers	m
$\boldsymbol{F}_f$	Darcy flux through grid face f	$m^3\ s^{-1}$
f	Grid face index	dimensionless
P	Primary cell index in the finite-volume stencil	dimensionless
t	Current time level	s
$t + \Delta t$	Next time level	s
Da	Damkohler number characterizing the ratio of reaction to transport time scales	dimensionless
PV_{BT}	Pore volume to breakthrough	PV
q_{inj}	Injection or displacement rate	$m^3\ s^{-1}$
T_{inj}	Injection temperature	K

References

1. Al-Shargabi, M.; Davoodi, S.; A.Wood, D.; Ali, M.; Rukavishnikov, S.V.; Minaev, M.K. A critical review of self-diverting acid treatments applied to carbonate oil and gas reservoirs. *Pet. Sci.* **2023**, *20*, 922–950. [CrossRef]
2. Shafiq, M.; Mahmud, H. Sandstone matrix acidizing knowledge and future development (Review). *J. Pet. Explor. Prod. Technol.* **2017**, *7*, 1205–1216. [CrossRef]
3. Du, J.; Yuan, Y.; Liu, P.; Wang, Q.; Liu, J.; Huang, Q. A review of self-generating acid system of high temperature reservoir. *Energy Sources Part A Recover. Util.* **2024**, *46*, 2059–2079. [CrossRef]
4. Liu, M.; Zhang, S.; Mou, J.; Zhou, F.; Shi, Y. Diverting mechanism of viscoelastic surfactant-based self-diverting acid and its simulation. *J. Pet. Sci. Eng.* **2013**, *105*, 91–99. [CrossRef]
5. Chang, T.; Jiang, Y.; Zhao, H.; Chen, X.; Mo, W. Effect of two-phase viscosity difference and natural fractures on the wormhole morphology formed by two-phase acidizing with self-diverting acid in carbonate rocks. *Phys. Fluids* **2024**, *36*, 093623. [CrossRef]

6. Chang, T.; Li, Y. Study on the uniform acidification mechanism of the self-diverting acid in the rock with multi-flow units based on the correct-hydro-temperature-chemical multiphysics coupling model. *Phys. Fluids* **2025**, *37*, 083613. [CrossRef]
7. Ratnakar, R.R.; Kalia, N.; Balakotaiah, V. Modeling, analysis and simulation of wormhole formation in carbonate rocks with in situ cross-linked acids. *Chem. Eng. Sci.* **2013**, *90*, 179–199. [CrossRef]
8. Nasr-El-Din, H.A.; Samuel, E.; Samuel, M. Application of a new class of surfactants in stimulation treatments. In *Proceedings of the SPE International Improved Oil Recovery Conference in Asia Pacific, Kuala Lumpur, Malaysia, 20–21 October 2003*; SPE: Richardson, TX, USA, 2003; p. SPE–84898.
9. Nasr-El-Din, H.A.; Samuel, M. Lessons learned from using viscoelastic surfactants in well stimulation. *Spe Prod. Oper.* **2007**, *22*, 112–120. [CrossRef]
10. Gomaa, A.M.; Cutler, J.; Qu, Q. An Effective Acid Placement Technique to Stimulate High-Temperature Sandstone and Carbonate Formations. In Proceedings of the 6th International Petroleum Technology Conference, Beijing, China, 26–28 March 2013.
11. Sibarani, T.T.; Ziauddin, M.; Nasr-El-Din, H.A.; Zakaria, A.S. The Impact of Pore Structure on Carbonate Stimulation Treatment Using VES-Based HCl. In Proceedings of the SPE Asia Pacific Oil and Gas Conference and Exhibition, Brisbane, Australia, 23–25 October 2018.
12. Li, S.; He, Y.; Cheng, Q.; Wu, W.; Yin, N.; Ren, H.; Chen, C.; Zhuo, S.; Long, Y. Influence of Heterogeneity on Acidizing Performance in Multi-Layered Carbonate Reservoirs. *Processes* **2025**, *13*, 3852. [CrossRef]
13. Yoo, H.; Kim, Y.; Lee, W.; Lee, J. An experimental study on acid-rock reaction kinetics using dolomite in carbonate acidizing (Article). *J. Pet. Sci. Eng.* **2018**, *168*, 478–494. [CrossRef]
14. Dong, K.; Zhu, D.; Hill, A.D. The role of temperature on optimal conditions in dolomite acidizing: An experimental study and its applications. *J. Pet. Sci. Eng.* **2018**, *165*, 736–742. [CrossRef]
15. Wang, Y. The Optimum Injection Rate for Matrix Acidizing of Carbonate Formations. In Proceedings of the SPE Annual Technical Conference and Exhibition, Houston, TX, USA, 3–6 October 1993.
16. Huang, T.; Hill, A.; Schechter, R. Reaction rate and fluid loss: The keys to wormhole initiation and propagation in carbonate acidizing. *Spe J.* **2000**, *5*, 287–292. [CrossRef]
17. Sayed, M.; Nasr-El-Din, H.A.; Nasrabadi, H. Reaction of emulsified acids with dolomite. *J. Can. Pet. Technol.* **2013**, *52*, 164–175. [CrossRef]
18. Sayed, M.; Chang, F. How Downhole Conditions Influence Acidizing Performance in Carbonate Reservoirs: An Experimental Study. *Spe J.* **2026**, *31*, 1467–1485. [CrossRef]
19. Dong, K.; Zhu, D.; Hill, A.D. Theoretical and experimental study on optimal injection rates in carbonate acidizing. *Spe J.* **2017**, *22*, 892–901.
20. Taylor, K.; Al-Ghamdi, A.; Nasr-El-Din, H. Effect of Additives on the Acid Dissolution Rates of Calcium and Magnesium Carbonates. *Spe Prod. Facil.* **2004**, *19*, 122–127. [CrossRef]
21. Taylor, K.; Nasr-El-Din, H.; Mehta, S. Anomalous Acid Reaction Rates in Carbonate Reservoir Rocks. *Spe J.* **2006**, *11*, 488–496. [CrossRef]
22. Weiren, M.; Yongming, L. Numerical Simulation Study on Wormhole Propagation Morphology in Fractured Carbonate Rocks during Acidizing. *E3S Web Conf.* **2025**, *639*, 01012. [CrossRef]
23. Kalia, N.; Balakotaiah, V. Effect of medium heterogeneities on reactive dissolution of carbonates. *Chem. Eng. Sci.* **2009**, *64*, 376–390. [CrossRef]
24. Chang, T.; Jiang, Y.; Li, Y.; Chen, X.; Kang, X.; Mo, W. Study on the effect of natural fractures and temperature on the wormhole morphology formed by two-phase acidizing in carbonate rocks. *Phys. Fluids* **2024**, *36*, 083333. [CrossRef]
25. Panga, M.K.; Ziauddin, M.; Balakotaiah, V. Two-scale continuum model for simulation of wormholes in carbonate acidization. *Aiche J.* **2005**, *51*, 3231–3248. [CrossRef]
26. Yang, G.; Wu, X.; Hou, J.; Zhou, F.; Nie, F. Study on the Influence of Heterogeneity of Low-Permeability Reservoirs on Wormhole Morphology and Acidizing Process Parameters. *Processes* **2024**, *12*, 2740. [CrossRef]
27. Samadi, F.; Esmaeilzadeh, F.; Mowla, D. Modeling of dissolution patterns for carbonate acidizing in the porous media. *Porous Media Its Appl. Sci. Eng. Ind.* **2012**, *1453*, 167. [CrossRef]
28. Jia, C.; Sepehrnoori, K.; Yao, J. Numerical Studies and Analysis on Reactive Flow in Matrix Acidizing Coupled Thermal-Hydrological-Mechanical-Chemical Processes. In Proceedings of the 55th U.S. Rock Mechanics/Geomechanics Symposium 2021, Houston, TX, USA, 20–23 June 2021.
29. Liu, P.; Yao, J.; Couples, G.D.; Huang, Z.; Sun, H.; Ma, J. Numerical modelling and analysis of reactive flow and wormhole formation in fractured carbonate rocks. *Chem. Eng. Sci.* **2017**, *172*, 143–157. [CrossRef]
30. Xue, H.; Huang, Z.; Zhao, L.; Wang, H.; Kang, B.; Liu, P.; Liu, F.; Cheng, Y.; Xin, J. Influence of acid-rock reaction heat and heat transmission on wormholing in carbonate rock. *J. Nat. Gas Sci. Eng.* **2018**, *50*, 189–204. [CrossRef]
31. Wang, C.; Xu, C.; Wang, X.; Tian, M.; Pei, E. Influence of Type and Concentration of Acid on Reaction Kinetics and Reservoir Permeability Enhancement in Tight Limestone Acidizing. *Processes* **2025**, *13*, 851. [CrossRef]

32. Samadi, F.; Esmaeilzadeh, F.; Mowla, D. 3-D Simulation of acid injection into a carbonate porous media: Nonlinear chemistry(Article). *J. Porous Media* **2013**, *16*, 959–966. [CrossRef]
33. Kalia, N.; Glasbergen, G. Wormhole formation in carbonates under varying temperature conditions. In *Proceedings of the SPE European Formation Damage Conference and Exhibition, Scheveningen, The Netherlands, 27–29 May 2009*; SPE: Richardson, TX, USA, 2009; p. SPE–121803.
34. Liu, P.; Xue, H.; Zhao, L.Q.; Fu, Y.; Luo, Z.; Qu, Z. Analysis and simulation of rheological behavior and diverting mechanism of in situ self-diverting acid. *J. Pet. Sci. Eng.* **2015**, *132*, 39–52. [CrossRef]
35. Carman, P.C. *Flow of Gas Through Porous Media*; Butterworths Scientific Publications: London, UK, 1956.

Disclaimer/Publisher's Note: The statements, opinions and data contained in all publications are solely those of the individual author(s) and contributor(s) and not of MDPI and/or the editor(s). MDPI and/or the editor(s) disclaim responsibility for any injury to people or property resulting from any ideas, methods, instructions or products referred to in the content.